Journal of Materials Chemistry A

COMMUNICATION

View Article Online
View Journal | View Issue

Cite this: J. Mater. Chem. A, 2019, 7, 13917

Received 6th March 2019
Accepted 19th May 2019

DOI: 10.1039/c9ta02444a

rsc.li/materials-a

Low-temperature electroless synthesis of mesoporous aluminum nanoparticles on graphene for high-performance lithium-ion batteries†

Hongyu Zhang,[a] Guanglin Xia, *[ab] Fang Fang,[a] Dalin Sun[a] and Xuebin Yu *[a]

The controllable fabrication of nanostructured Al at low temperature remains a great challenge for extending its application into emerging areas such as energy storage. Herein, we report a green and controllable electroless synthesis of mesoporous Al nanoparticles on graphene (mp-Al@G) using nontoxic Mg nanoparticles (NPs) and molten $AlCl_3$ at a temperature as low as 190 °C. Moreover, the removal of the by-product ($MgCl_2$) leads to the formation of mesopores inside the Al NPs, which are uniformly distributed on the graphene. The composite exhibits high reversible capacity and long cycle life when used as the anode material in lithium ion batteries. When coupled with a $LiNi_{0.6}Co_{0.2}Mn_{0.2}O_2$ cathode, the full cell could also deliver an energy density of 455 W h kg^{-1} at a 1C rate, which demonstrates its potential application in high energy lithium ion batteries. These findings will trigger more investigations into developing Al as a high-performance energy storage material.

Introduction

Aluminum has been identified as one of the promising next-generation anodes for lithium-ion batteries (LIBs), owing to its high theoretical capacity (2234 mA h g^{-1} considering the formation of Li_9Al_4), low potential plateau (~0.19–0.45 V against Li^+/Li), and high electrical conductivity.[1,2] More importantly, Al is the most abundant metal and the third most abundant element in the Earth's crust, which has been widely applied in the aerospace, transportation, and building industries, making it the second most produced metal in the modern world.[3] The development of Al anode materials for LIBs is still in its infancy, however, due to its fast capacity fade (<200 mA h g^{-1} after 20 cycles), which is mainly attributed to the huge volume change during the lithium storage process, leading to serious cracking of Al and the continuous generation of a very thick solid electrolyte interphase (SEI) film on the Al surface. One effective strategy to improve the electrochemical properties of Al anode materials is to build nanostructures, which could not only improve the electrochemical activity of Al due to the shortened diffusion pathways of Li ions, but also retard particle fragmentation through mitigating the internal strain induced during the alloying and dealloying process to some extent.[4–6] Unfortunately, the fabrication of nanostructured Al is significantly limited by its very high native reduction potential (−1.67 V *vs.* the standard hydrogen electrode (SHE)). The high reactivity of Al leads to the easy formation of a compact and stable Al oxide, which has been demonstrated to be a good insulating barrier to both electrons and Li ions (2.7×10^{-14} cm^2 s^{-1} at 600 °C) and hence could detrimentally passivate the surface reactivity towards lithium storage and extraction.[7] What is worse is the significant increase of oxide content as the particle size decreases, and hence, aluminum oxide could account for 60% or more of the mass in a particle 50 nm or less in diameter.[8–10] Since the oxide is electrochemically inactive, the naturally formed oxide layer further results in much lower electrochemical capacity of the whole system due to the introduced dead weight.

Metallic Al has been conventionally synthesized *via* electrochemical deposition by the Hall–Heroult process at a high temperature of 960 °C using carbon as the anode and the Al pool as the cathode.[11] It thus requires high energy consumption and a stringent reaction environment, accompanied by serious emission of greenhouse gases, which greatly limits its wide application in the fabrication of nanostructured Al-based anode materials. Recently, it has been reported that Al could be fabricated through the reduction of $AlCl_3$ using Mg.[12,13] Inspired by this result, herein we report a facile strategy for the preparation of mesoporous Al nanoparticles (NPs) by a graphene-supported electroless reaction between molten $AlCl_3$ and Mg NPs. Compared with the traditional method to fabricate Al metals, the electroless reduction of $AlCl_3$ with Mg could occur at

[a]Department of Materials Science, Fudan University, Shanghai 200433, China. E-mail: xiaguanglin@fudan.edu.cn; yuxuebin@fudan.edu.cn

[b]Institute for Superconducting and Electronic Materials, University of Wollongong, North Wollongong, NSW 2522, Australia

† Electronic supplementary information (ESI) available. See DOI: 10.1039/c9ta02444a

a much lower temperature of 190 °C, and provide better control over the particle size and morphology of the as-synthesized Al by using Mg as the both the reductant and a self-sacrificing template. Furthermore, Mg is nontoxic, so using it as the reducing agent could effectively reduce the safety risks of the synthesis procedure. More interestingly, the removal of the $MgCl_2$ that is formed during the electroless reduction could leave open channels in the as-synthesized Al, resulting in the formation of mesoporous Al NPs uniformly distributed on graphene (mp-Al@G). In addition, the homogeneous introduction of graphene, which serves as a robust structural support and electronic pathway, could alleviate the aggregation and coalescence of Al nanoparticles and enhance the ion transport through the electrode. This strategy provides a green and controllable approach for scalable production of high-performance Al anodes.

Results and discussion

The electroless fabrication of mp-Al@G is schematically illustrated in Fig. 1a. Typically, graphene-supported MgH_2 NPs (MgH_2@G) were first fabricated through a hydrogen-induced assembly process involving dibutyl magnesium (Fig. S1a in the ESI†).[14] The resulting MgH_2 NPs were then transformed into Mg NPs uniformly distributed on the graphene (Mg@G) with a particle size of 40–100 nm (Fig. 1b) *via* a simple heating process induced by the favorable adsorption of both dibutyl magnesium and MgH_2 NPs on graphene. The interplanar-spacing of 2.45 Å corresponding to the (101) planes of Mg in the high-resolution transmission electron microscope (HRTEM) image of Mg@G (inset of Fig. 1b) clearly manifests the formation of Mg, coinciding well with the X-ray diffraction (XRD) result (Fig. S1b†). The porous structure of Mg@G, resulting from the assembly of alternating layers of Mg NPs and graphene stacks, provides facile pathways for the homogeneous infiltration of molten $AlCl_3$ (Fig. S2†), while the homogeneous Mg NPs, acting as self-sacrificing templates, are capable of guiding the *in situ* formation of Al NPs on the stable structural support of graphene. Subsequently, a thermal treatment was carried out at 190 °C to infiltrate the molten $AlCl_3$ into the porous structure of Mg@G, and Al was generated *in situ* through the electroless reaction between Mg and $AlCl_3$, *i.e.*, $3Mg + 2AlCl_3 = 3MgCl_2 + 2Al$, as evidenced by the XRD results (Fig. S1c†). After the removal of $MgCl_2$ *via* washing, the XRD results confirmed the formation of pure Al phases in the resulting mp-Al@G (Fig. S1d†).

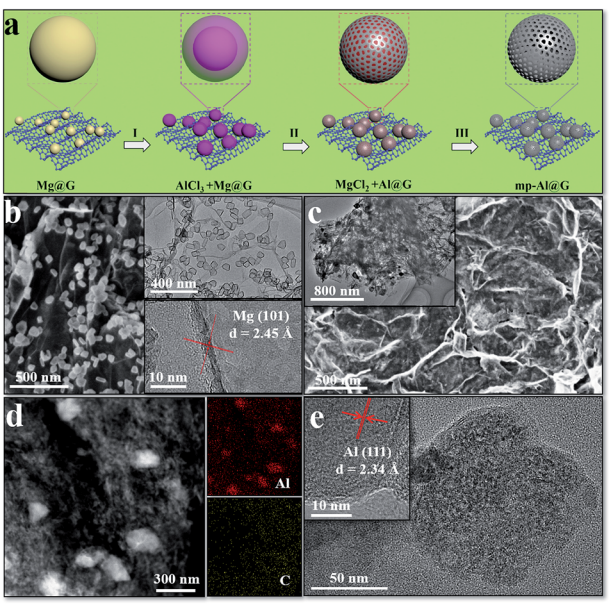

Fig. 1 (a) Schematic illustration of the electroless synthesis of mp-Al@G: (I) infiltration of molten $AlCl_3$, (II) electroless reduction, and (III) removal of $MgCl_2$. (b) SEM, TEM, and HRTEM images of Mg@G. (c) SEM, (d) representative scanning TEM (STEM) image and the corresponding elemental mapping, and (e) TEM image of mp-Al@G. The insets show higher magnification.

The field-emission scanning electron microscope (FE-SEM) and transmission electron microscope (TEM) images illustrate that, owing to the structural support role of graphene with Mg NPs as the self-sacrificing template, the as-synthesized mp-Al@G inherits the morphology of Mg@G, and the resulting Al NPs are uniformly distributed on graphene (Fig. 1c). The scanning TEM (STEM) image and the corresponding elemental mapping (Fig. 1d) provides further evidence for the uniform dispersion of Al NPs on graphene with enlarged particle sizes ranging from 70 to 200 nm due to the large volume expansion involved in the reaction between Mg and $AlCl_3$. Interestingly, mesopores are clearly observed inside the Al NPs (Fig. 1e), which could be attributed to the voids left by the removal of $MgCl_2$, leading to the formation of mesoporous Al NPs uniformly supported on graphene. Brunauer–Emmett–Teller (BET) measurements identified the significant increase in the surface area and pore volume after the transformation of Mg@G to mp-Al@G, as well as the widened pore size distribution from 4 to 12 nm, which provides further evidence of the formation of mesoporous Al NPs on graphene (Fig. S3 and S4†). The mesoporous structure of Al NPs could not only accommodate the volume changes during the lithiation and delithiation in the course of cycling, but also provide more facile pathways for the diffusion of Li^+.

The HRTEM image of mp-Al@G (inset of Fig. 1e) presents clear lattice fringes with a *d*-spacing of 2.34 Å indexed to the (111) planes of Al, in good agreement with the XRD results, which confirms the formation of mp-Al NPs. It should be noted that there are no obvious amorphous layers belonging to aluminum oxide, which is usually present on the surface of Al NPs in a large amount, resulting from their high reactivity (Fig. S5†), that can be observed on the surfaces of the mp-Al NPs. The full X-ray photoelectron spectroscopy (XPS) spectrum validates the presence of only Al, C, and a trace amount of O in mp-Al@G (Fig. S6†), demonstrating the complete removal of $MgCl_2$. Moreover, the high-resolution Al 2p spectrum of mp-Al@G (Fig. S7†) exhibits a much stronger peak of metallic Al (73.7 eV) than that of Al_2O_3 (75.3 eV),[15–17] which validates the synthesis of Al NPs with high purity through a simple and scalable electroless reaction at moderate temperature. The amount of Al in mp-Al@G is calculated to be 38 wt% from the thermogravimetric analysis (TGA) curve (Fig. S8†). The corresponding elemental mapping (Fig. 1d) also verifies the uniform dispersion of mesoporous Al NPs on graphene in mp-Al@G. Meanwhile, the

Raman spectrum of mp-Al@G shows a more intensified D band at 1342 cm^{-1} than the G band at 1586 cm^{-1} (Fig. S9†), indicating the presence of graphene with a disordered structure, which could further facilitate the transfer of Li^+.[18]

The electrochemical performance of mp-Al@G was first examined by cyclic voltammetry (CV) measurements. The broad peak at 0.7 V in the first cycle is attributed to the formation of SEI layers.[19] The reduction peak at 0.16 V and the oxidation peak at 0.5 V (Fig. 2a) correspond to the alloying and de-alloying of the Al anode in the lithiation and delithiation processes, respectively.[4,6] This result is in accordance with the lithiation/delithiation plateaus at around 0.2 V and 0.5 V, respectively, in the galvanostatic discharge–charge voltage profiles. In addition, there are pronounced voltage dips before the stable plateau for the lithiation of both Al NPs and a ball-milled composite Al NP and graphene (denoted as BM Al–G) electrode (inset of Fig. 2b). This mainly results from a poor thermodynamic driving force for the lithiation of Al due to the induced large elastic strain during the formation of Li–Al alloys, and hence, a higher electrochemical driving force is required.[20] No voltage dip in the lithiation process of mp-Al@G is observed (Fig. 2b), however, indicating that the mesoporous structure of Al NPs in mp-Al@G could effectively mitigate the elastic strain during the lithiation process and promote the lithium storage kinetics. The first discharge and charge capacities of mp-Al@G reached 1461 mA h g^{-1} and 1059 mA h g^{-1}, respectively, with an initial coulombic efficiency of 72.5%. It should be noted that the specific capacities of the mp-Al@G electrode in this work were calculated based on the total mass of Al and graphene. The capacity loss of mp-Al@G in the first cycle could be attributed to the formation of a SEI and some irreversible reactions on the surface of graphene and mp-Al NPs, as verified by the characteristic plateau at around 0.7 V (Fig. S10†),[6,21–23] which could also be observed in the initial discharge process of graphene obtained from mp-Al@G after the removal of Al (Fig. S11a†). Upon the proceeding of the charge–discharge process, this plateau was clearly weakened after 5 cycles, leading to a rapid increase of coulombic efficiency to 99.2% (Fig. S10†). After 100 cycles, the reversible capacity of mp-Al@G is still as high as 1020 mA h g^{-1}, corresponding to a capacity retention of 91% compared with the third cycle, while only a specific capacity of lower than 400 mA h g^{-1} could be achieved for graphene after 40 cycles (Fig. S11b†). In comparison, with the increase of the loading ratio of Al to 70%, although a higher discharge capacity of 1684 mA h g^{-1} was obtained for mp-Al@G in the initial cycle, the reversible specific capacity rapidly decays to only 507 mA h g^{-1} (Fig. S12†). This could be mainly attributed to the severe growth and aggregation of mesoporous Al nanoparticles, and the inhomogeneous distribution of Al particles on graphene (Fig. S13†) due to the large particle size and the inhomogeneous distribution of Mg on graphene as the precursor and the significant volume expansion involved in the reduction of $AlCl_3$ (Fig. S13a and b†). In strong contrast, the initial charge capacities of the Al NPs and BM Al–G are only 420 and 810 mA h g^{-1}, respectively, and the reversible capacity rapidly decays to 128 mA h g^{-1} and 340 mA h g^{-1} for the Al NPs and BM Al–G, respectively, after only 100 cycles, which is attributed to the significant volume changes (Fig. 2c). This indicates that the mesoporous structure of Al NPs with their uniform dispersion on graphene is capable of accommodating the volume changes and thus improving the reversibility of the Al anode during the discharging/charging process. Furthermore, the mp-Al@G electrode exhibited excellent rate capabilities even at high current densities (Fig. 2d and S14†). Specifically, when the current densities were increased from 0.2 A g^{-1} to 0.5, 1, 2, 3, and 5 A g^{-1}, the mp-Al@G could deliver specific capacities of 1012, 926, 876, 752, 672, and 587 mA h g^{-1}, respectively. When the current density returned from 5 A g^{-1} to 0.2 A g^{-1}, the specific capacity of mp-Al@G could recover, suggesting the high lithium storage kinetics of mp-Al@G with excellent reversibility. At a high rate of 2 A g^{-1}, a high reversible capacity of 735 mA h g^{-1} could still be achieved for mp-Al@G after 300 cycles, which is much higher than that for Al NPs (45 mA h g^{-1}) and BM Al–G (240 mA h g^{-1}) under the same conditions (Fig. 2e). To the best of our knowledge, such high electrochemical performance of this mp-Al@G electrode compares favorably with that of some previously reported alloying-based anodes (*e.g.*, Si, Ge, and Sn) (Table S1†).

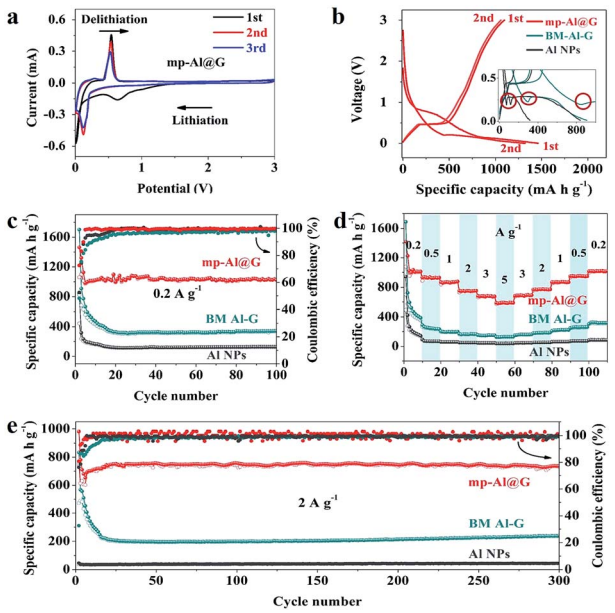

Fig. 2 Electrochemical properties of mp-Al@G, BM Al–G, and reference Al NPs. (a) Cyclic voltammograms of mp-Al@G. (b) The first two discharge–charge profiles at 0.2 A g^{-1}, with the inset showing the dips before the voltage plateaus for BM Al–G and Al NPs. (c) Cycling performance and coulombic efficiency at 0.2 A g^{-1}. (d) Rate capabilities. (e) Cycling performance and coulombic efficiency at 2 A g^{-1}.

To determine the origin of the superior rate performance of mp-Al@G, the pseudocapacitive behavior and pseudocapacitive-like contribution of mp-Al@G were investigated based on the CV curves (Fig. S15†). The current (i) has a power law relationship with the scan rate (v):[24–26]

$$i = av^b \quad (1)$$

where a and b are adjustable constants and the b-value could be obtained through the slope of the linear fitting of the log(i) *versus* log(v) plot. The b-value is an estimate of the type of charge

storage occurring in the electrode: if b is 0.5, then the current is diffusion-controlled; if b is 1, the current is surface-controlled (capacitive). The b-values for the anodic and cathodic peaks are calculated to be 0.76 and 0.82 (Fig. S16†), respectively, indicating that surface-controlled kinetics of the mp-Al@G electrode is favored. The capacitive contribution to the capacity of the mp-Al@G electrode is calculated to be 61.9% at 0.1 mV s^{-1} (Fig. S17a†), and with increasing scan rate, the capacitive contribution could reach 84.5% at a high scan rate of 0.8 mV s^{-1} (Fig. S17b–d†). This clearly demonstrates that the capacitive behavior is the dominant contributor to the capacity at high scan rates for the mp-Al@G electrode (Fig. S18†), owing to the mesoporous structure of Al NPs, where the electrolyte could readily access the entire surface for the rapid transfer of Li^+ into the electrode, leading to the excellent high-rate performance of mp-Al@G.[27]

Electrochemical impedance spectroscopy (EIS) was further adopted to understand the mechanism for the favorable cycling capability of mp-Al@G (Fig. S19†). Each impedance spectrum comprises two depressed semicircles at high and medium frequencies and one oblique line in the low frequency region, which are related to the charge-transfer process and lithium ion transfer, respectively. The charge-transfer resistance (R_{ct}), which is a key indicator for the kinetics of the electrode, is calculated to be only 112.7 Ω for the mp-Al@G electrode (Fig. S20†), much lower than that of the BM Al–G electrode (138.5 Ω). Moreover, after 100 cycles, only a slight increase in R_{ct} to 130.3 Ω is observed for the mp-Al@G electrode, while this value is significantly increased to 188.4 Ω for the BM Al–G electrode (Table S2†). This indicates that the homogeneous distribution of mp-Al NPs with high purity on graphene could tremendously accelerates the electron transfer and the kinetics for Li ion transport of the electrode, leading to outstanding electrochemical performance. In addition, the mesoporous structure of Al NPs under the structural support of graphene could efficiently accommodate the elastic stress induced by the large volume changes, leading to excellent cycling stability (Fig. 3a). As shown in the SEM images of cycled electrodes, compared with the fresh electrode (Fig. 3b_1 and b_2), the mp-Al@G electrode (Fig. 3c_1 and d_1) maintains its large-scale compact and flat surface with few visible cracks, even after 100 cycles. In contrast, there are obvious cracks on the electrode surface of Al NPs after 100 cycles at a small current density of 0.2 A g^{-1} (Fig. S21b_1†), and the electrode surface is even worse, with plentiful large cracks and some distinct parts peeled-off from the electrode, when the current density further increases to 0.5 A g^{-1} (Fig. S21c_1†). Moreover, the increase in the electrode thickness of mp-Al@G after 100 cycles at 0.2 A g^{-1} and 0.5 A g^{-1} was measured to be only 10% and 47%, respectively (Fig. 3c_2 and d_2), which is also much lower than for the Al NP electrodes (60% and 176%, respectively) (Fig. S21a_2–c_2†). After cycling, the uniform distribution of Al and C is well preserved in the mp-Al@G electrode, while the obvious aggregation of active materials could be easily viewed from the element mapping of the Al NP electrode. Furthermore, no distinct aggregation can be observed from the TEM image of mp-Al@G after 100 cycles at 0.5 A g^{-1} (Fig. S22 and S23†). All these results demonstrate the superior structural stability of mp-Al@G, which effectively enhances the cycle life.

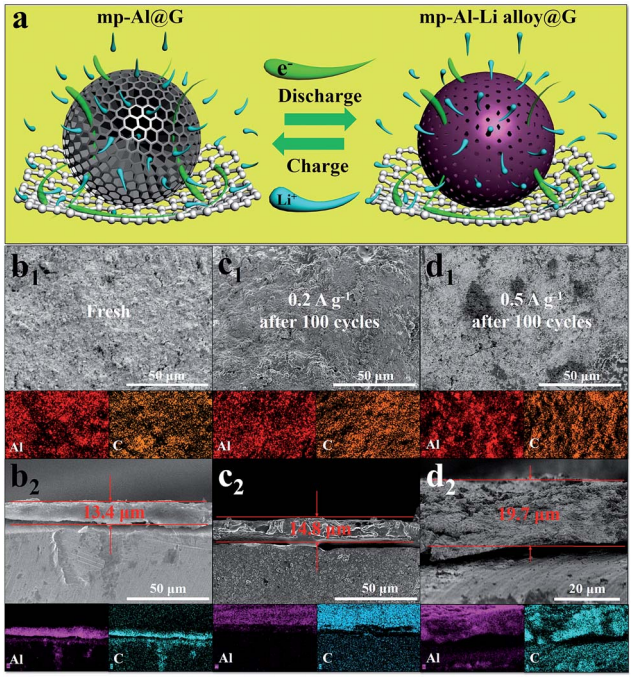

Fig. 3 (a) Schematic illustration of the reversible lithium storage process of the mp-Al@G electrode. SEM images and the corresponding element mappings of the mp-Al@G electrode in various states: (b_1 and b_2) initial state, (c_1 and c_2) after 100 cycles at 0.2 A g^{-1}, and (d_1 and d_2) after 100 cycles at 0.5 A g^{-1}.

The potential application of mp-Al@G was further investigated by constructing full cells with commercial $LiNi_{0.6}Co_{0.2}Mn_{0.2}O_2$ (NCM) as the cathode (Fig. 4a). The average operating voltage of NCM is over 4.0 V in half cells at 0.2C with an initial discharge capacity of 190 mA h g^{-1} (Fig. 4b) and good rate capability (Fig. S24†). As a result, because of the alloying and dealloying voltages of Al at around 0.2 V and 0.5 V, the assembled mp-Al@G//NCM full cells display a slightly lower average voltage of 3.5 V at 0.2C from 2.4 V to 4.4 V (Fig. 4c). Three mp-Al@G//NCM full cells were capable of powering 29 red light-emitting diode (LED) lamps (Fig. 4d), which directly

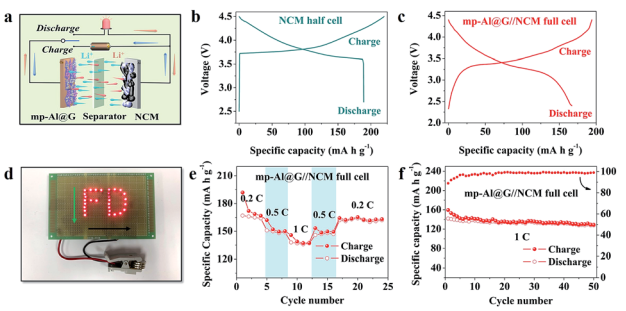

Fig. 4 (a) Schematic illustration of the mp-Al@G electrode in a full cell using $LiNi_{0.6}Co_{0.2}Mn_{0.2}O_2$ as the cathode. (b) Voltage profiles of $LiNi_{0.6}Co_{0.2}Mn_{0.2}O_2$ in a half cell at 0.2C. (c) Voltage profiles of mp-Al@G//NCM at 0.2C. (d) Digital image of 29 red LEDs lit by three mp-Al@G//NCM full cells. (e) Rate performance of the full cell. (f) High-rate cycling performance of mp-Al@G//NCM.

demonstrates that the working voltage of mp-Al@G//NCM is over 3.5 V (working voltage of one red LED: 1.5 V). The first charge and discharge capacities of this full cell are 194 and 167 mA h g^{-1}, respectively, corresponding to a coulombic efficiency of 86% (note that the specific capacity of full cells is calculated based on the total mass of cathode and anode materials). Furthermore, this full cell exhibits excellent rate capability, retaining 91% and 81% of the capacity (0.2C) at 0.5C and 1C, respectively, and it could return to approximately 161 mA h g^{-1} when the current density decreased to 0.2C (Fig. 4e and S25†). More importantly, the mp-Al@G//NCM full cell delivered a specific capacity of 130 mA h g^{-1}, corresponding to 81% of the initial capacity, after 50 cycles with an average coulombic efficiency of 99% (Fig. 4f and S26†). In addition, taking the anode and cathode materials into account for calculation of the energy density (ED) based on the equation: ED $= C_{(\text{cathode+anode})} \times V_{\text{nominal}}$, the specific energy density of mp-Al@G//NCM full cells ($C_{(\text{cathode+anode})}$ = 130 mA h g^{-1} and $V_{\text{nominal}} = 3.5$ V) at 910 W kg^{-1} could reach 455 W h kg^{-1}, which is much higher than for most LIBs, while only an ED of 391 W h kg^{-1} could be achieved for graphene//NCM full cells based on the same method (Fig. S27†). These results provide direct evidence of the promising potential of mp-Al@G as a high energy density anode for LIBs.

Conclusions

In summary, we have developed a low-temperature electroless reduction strategy for fabricating mesoporous Al NPs with high purity, which are homogeneously distributed on graphene, by using Mg NPs as self-sacrificing templates. The mp-Al@G electrode exhibits excellent electrochemical performance, which is attributable to the mesoporous structure of Al NPs and the structural support role of graphene. More importantly, with NCM as the cathode, the energy density of the full cell could reach 455 W h kg^{-1}. The present study not only overcomes the major challenges of Al-based anode materials, but also provides a facile and controllable way to synthesize nanostructured Al with lower energy consumption under moderate conditions, which is of high interest and importance for many other emerging applications.

Conflicts of interest

There are no conflicts to declare.

Acknowledgements

This work was partially supported by the National Science Fund for Distinguished Young Scholars (51625102), the National Natural Science Foundation of China (51571063 and 51831009), the Innovation Program of Shanghai Municipal Education Commission (2019-01-07-00-07-E00028), the Science and Technology Commission of Shanghai Municipality (17XD1400700), and a Discovery Early Career Researcher Award (DE170100362) from the Australian Research Council (ARC). The authors also would like to thank Dr Tania Silver for critical reading of the manuscript.

References

1 Y. Hamon, T. Brousse, F. Jousse, P. Topart, P. Buvat and D. M. Schleich, *J. Power Sources*, 2001, **97–98**, 185.
2 N. Nitta and G. Yushin, *Part. Part. Syst. Charact.*, 2014, **31**, 317.
3 G. D. Kwon, E. Moyen, Y. J. Lee, J. Joe and D. Pribat, *ACS Appl. Mater. Interfaces*, 2018, **10**, 29486.
4 S. Li, J. Niu, Y. C. Zhao, K. P. So, C. Wang, C. A. Wang and J. Li, *Nat. Commun.*, 2015, **6**, 7872.
5 J. H. Park, C. Hudaya, A. Y. Kim, D. K. Rhee, S. J. Yeo, W. Choi, P. J. Yoo and J. K. Lee, *Chem. Commun.*, 2014, **50**, 2837.
6 X. Chang, Z. Xie, Z. Liu, X. Zheng, J. Zheng and X. Li, *Nano Energy*, 2017, **41**, 731.
7 S. Hao and C. Wolverton, *J. Phys. Chem. C*, 2013, **117**, 8009.
8 T. J. Foley, C. E. Johnson and K. T. Higa, *Chem. Mater.*, 2005, **17**, 4086.
9 M. J. Meziani, C. E. Bunker, F. Lu, H. Li, W. Wang, E. A. Guliants, R. A. Quinn and Y.-P. Sun, *ACS Appl. Mater. Interfaces*, 2009, **1**, 703.
10 B. W. McMahon, J. Yu, J. A. Boatz and S. L. Anderson, *ACS Appl. Mater. Interfaces*, 2015, **7**, 16101.
11 S. Prasad, *J. Braz. Chem. Soc.*, 2000, **11**, 245.
12 N. Lin, Y. Han, L. Wang, J. Zhou, J. Zhou, Y. Zhu and Y. Qian, *Angew. Chem., Int. Ed.*, 2015, **127**, 3893.
13 N. Lin, Y. Han, J. Zhou, K. Zhang, T. Xu, Y. Zhu and Y. Qian, *Energy Environ. Sci.*, 2015, **8**, 3187.
14 Y. Q. Huang, G. L. Xia, J. Chen, B. P. Zhang, Q. Li and X. B. Yu, *Prog. Nat. Sci.*, 2017, **27**, 87.
15 S. C. Reiff and J. A. LaVerne, *Radiat. Phys. Chem.*, 2017, **131**, 46.
16 W. Lu, Y. Iwasa, Y. Ou, D. Jinno, S. Kamiyama, P. M. Petersen and H. Ou, *RSC Adv.*, 2017, **7**, 8090.
17 X. Xiao, P. Lu and D. Ahn, *Adv. Mater.*, 2011, **23**, 3911.
18 S. Zhang, L. Zhu, H. Song, X. Chen and J. Zhou, *Nano Energy*, 2014, **10**, 172.
19 Y. Huang, X. Lin, Q. Pan, Q. Li, X. Zhang, Z. Yan, X. Wu, Z. He and H. Wang, *Electrochim. Acta*, 2016, **193**, 253.
20 R. Kali, S. Badjate and A. Mukhopadhyay, *J. Appl. Electrochem.*, 2017, **47**, 479.
21 W. Ai, J. Jiang, J. Zhu, Z. Fan, Y. Wang, H. Zhang, W. Huang and T. Yu, *Adv. Energy Mater.*, 2015, **5**, 1500559.
22 Z.-S. Wu, W. Ren, L. Xu, F. Li and H.-M. Cheng, *ACS Nano*, 2011, **5**, 5463.
23 S.-L. Chou, J.-Z. Wang, M. Choucair, H.-K. Liu, J. A. Stride and S.-X. Dou, *Electrochem. Commun.*, 2010, **12**, 303.
24 B. K. Lesel, J. S. Ko, B. Dunn and S. H. Tolbert, *ACS Nano*, 2016, **10**, 7572.
25 V. Augustyn, J. Come, M. A. Lowe, J. W. Kim, P.-L. Taberna, S. H. Tolbert, H. D. Abruña, P. Simon and B. Dunn, *Nat. Mater.*, 2013, **12**, 518.
26 D. Chao, P. Liang, Z. Chen, L. Bai, H. Shen, X. Liu, X. Xia, Y. Zhao, S. V. Savilov, J. Lin and Z. X. Shen, *ACS Nano*, 2016, **10**, 10211.
27 C. Zhao, C. Yu, M. Zhang, H. Huang, S. Li, X. Han, Z. Liu, J. Yang, W. Xiao, J. Liang, X. Sun and J. Qiu, *Adv. Energy Mater.*, 2017, **7**, 1602880.